Unraveling spin density wave order in layered nickelates $La_3Ni_2O_7$ and $La_2PrNi_2O_7$ via neutron diffraction

Igor Plokhikh,[1,2,3,*] Thomas J. Hicken,[1,†] Lukas Keller,[1] Vladimir Pomjakushin,[1] Samuel H. Moody,[1] Pascale Foury-Leylekian,[4] Jonas J. Krieger,[1] Hubertus Luetkens,[1] Zurab Guguchia,[1] Rustem Khasanov,[1,‡] and Dariusz Jakub Gawryluk[1,§]

[1]*PSI Center for Neutron and Muon Sciences, Paul Scherrer Institute, Forschungsstrasse 111, 5232 Villigen, Switzerland*
[2]*Physics Department, Technical University Dortmund, Otto-Hahn-Straße 4, 44227 Dortmund, Germany*
[3]*Research Center "Future Energy Materials and Systems", 44227 Dortmund, Germany*
[4]*Université Paris-Saclay, CNRS, Laboratoire de Physique des Solides, 91405 Orsay, France*

(Received 8 November 2025; accepted 22 June 2026; published 7 August 2026)

The observation of pressure-induced superconductivity in two- and three-layer Ruddlesden-Popper nickelates has spurred intense interest in these materials as a platform for exploring unconventional superconductivity. While the ground state of these systems has been shown to exhibit magnetism, the direct determination of their magnetic structure remains elusive. This is a crucial aspect, as magnetism may play a role in the pairing mechanism of superconductivity in these materials. In this study, we resolve the magnetic structures in the bilayer (2222) polymorphs of $La_3Ni_2O_7$ and $La_2PrNi_2O_7$ compounds, using a combination of complementary techniques, namely, neutron powder diffraction and muon-spin rotation/relaxation (μSR). Magnetic neutron scattering in both samples emerges below ~150 K and is observed at the $(q_x, \frac{1}{2}, 0)$ position, with $q_x = 0$ and $\frac{1}{2}$ for $La_3Ni_2O_7$ and $q_x = 0$ for $La_2PrNi_2O_7$. Alternating low-magnetic-moment (0.05–0.075μ_B) and high-magnetic-moment (0.66μ_B) stripes form a single layer; the bilayers are formed through antiferromagnetic stacking of single layers along the out-of-plane direction. The magnetic scattering with two propagation vectors $q_x = 0$ and $\frac{1}{2}$ in the undoped $La_3Ni_2O_7$ is attributed to two magnetic stacking polymorphs within a single crystallographic phase. The magnetic structures are substantiated by the μSR spectra. These findings provide a detailed understanding of the magnetic ground state in bilayer nickelates, offering crucial insights into the possible precursor states that may influence the emergence of superconductivity in these materials.

DOI: 10.1103/rw8k-tng5

I. INTRODUCTION

$La_3Ni_2O_{7-\delta}$ and related layered nickelate systems have recently garnered significant attention due to their discovery as high-temperature superconductors under high pressure, marking this group as one of the few transition-metal-oxide-based superconductors alongside the well-known copper- and iron-based families [1–7]. This material's remarkable ability to exhibit superconductivity at temperatures exceeding 80 K under elevated pressure has opened a new frontier in the search for unconventional superconducting mechanisms. The complex phase diagram of $La_3Ni_2O_{7-\delta}$, analogous to that of cuprates and iron pnictides, which features an intricate interplay of electronic correlations, spin density waves (SDWs) and multiple charge density waves (CDWs), and pressure-induced structural transitions (Fig. 1; Fig. S1 of the Supplemental Material [8]), renders it a fascinating field for further detailed explorations. This constitutes Ruddlesden-Popper (RP)-type nickelates a potentially significant subject in the broader context of understanding high-temperature superconductivity.

The RP layered structure, reminiscent of the structure found in cuprates, is a crucial component in establishing its emerging phenomena [9]. At ambient pressure, in $La_3Ni_2O_{7-\delta}$ two orthorhombic crystallographic polymorphs—bilayer (2222) or alternating single trilayer (1313)—were reported [10–12]. Suppression of the orthorhombic distortion in the bilayer polymorph toward higher symmetry structures (*Fmmm* or *I*4/*mmm*; Fig. S2 of the Supplemental Material [8]) is a prerequisite for the onset of superconductivity [2,12,14]. The concurrent formation of the 1313 modification is proposed to be the reason for the filamentary and not bulk nature of superconductivity in $La_3Ni_2O_{7-\delta}$ [5]. The formation of the 1313 phase can be suppressed by partial substitution of La with Pr, to form a $La_{3-x}Pr_xNi_2O_{7-\delta}$ solid-solution series, while preserving the parent orthorhombic structure up to $x = 1$. This substitution yields the samples exhibiting bulk superconductivity [5].

The complex nature of the strongly correlated $La_3Ni_2O_{7-\delta}$ has been investigated using a variety of experimental probes, including resonant inelastic x-ray scattering [13], resonant

*Contact author: igor.plokhikh@psi.ch
†Contact author: thomas.hicken@psi.ch
‡Contact author: rustem.khasanov@psi.ch
§Contact author: dariusz.gawryluk@psi.ch

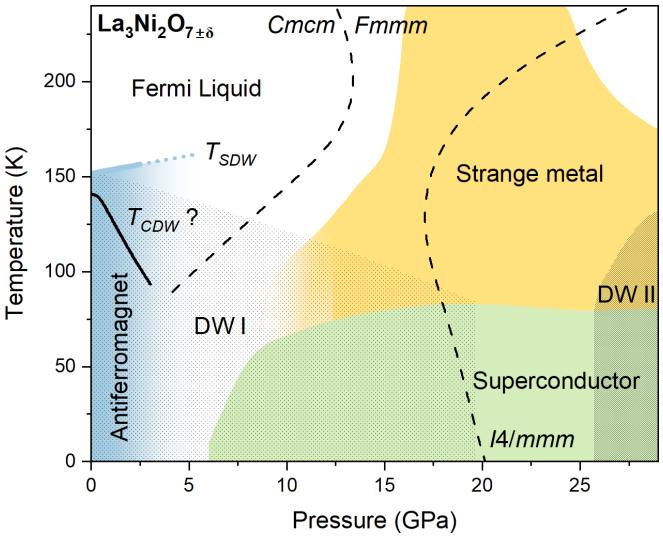

FIG. 1. Temperature-pressure phase diagram of bulk $La_3Ni_2O_{7-\delta}$. Solid and dashed lines represent the borders between different crystallographic phases; yellow, blue, green, and shaded coloring represent the phases sorted by their physical properties. DW, density wave. Based on Refs. [2–4,14–19]. A more detailed version of this figure, including specific data points and references, is available in the Supplemental Material (Fig. S1) [8].

soft x-ray scattering [20], x-ray absorption spectroscopy [21], ultrafast optical pump-probe spectroscopy [16], muon-spin rotation/relaxation (μSR) [18,22], and nuclear magnetic resonance [23,24]. The resonant x-ray studies have identified SDWs at low temperatures and ambient pressure, with an in-plane wave vector (0.25, 0.25), hinting at complex magnetic interactions within the material [13,20]. However, the exact magnetic structure for bulk $La_{3-x}Pr_xNi_2O_{7-\delta}$ ($x = 0$ and 1) has not been experimentally derived up to now. While high-pressure studies of $La_3Ni_2O_{7-\delta}$ have confirmed its superconducting phase, the connection between its magnetic and superconducting properties is still under investigation. So far, the actual ground state, the role of magnetic fluctuations, and their potential relationship with the superconducting pairing mechanism remain an open question [25–28]. Consequently, in the present study, the primary focus is directed toward the magnetic structure determination of the $La_{3-x}Pr_xNi_2O_7$ ($x = 0$ and 1).

Although $La_3Ni_2O_{7-\delta}$ has been the subject of neutron scattering studies [29–31], the precise nature of its magnetic order remained unclear up to now. In the related trilayer phase $La_4Ni_3O_{10}$, magnetic order has been observed via neutron scattering only in single crystals, as the magnetic signal is substantially weaker than the nuclear scattering [32]. Growing large high-quality single crystals of $La_3Ni_2O_{7-\delta}$ is challenging due to the coexistence of the 1313 and 2222 polymorphs [10–12], complicated by concurrent epitaxial intergrowth with other homologs ($La_{n+1}Ni_nO_{3n+1}$, $n = 1, 3, \infty$). The incorporation of the mono- and three-layer fragments in the otherwise consistent stacking of bilayers can be seen as a stacking fault; the pristine $La_3Ni_2O_7$ suffers notoriously from this. As a result, determining the magnetic structure of the pure 2222 phase is both critical and difficult. In this study, using high-intensity neutron powder diffraction (NPD), we detect Bragg scattering linked to the long-range spin density wave in $La_{3-x}Pr_xNi_2O_{7-\delta}$ ($x = 0$ and 1) and propose spin-structure models consistent with both neutron and μSR data. The findings presented herein are, therefore, of significance for the elucidation of the electronic structure of $La_3Ni_2O_{7-\delta}$ and its position within the broader family of transition-metal-oxide superconductors, thereby providing a foundation for further studies into its superconducting and magnetic behavior.

II. RESULTS

A. Basic characterization

According to x-ray powder diffraction [Fig. 2(a); Fig. S3 of the Supplemental Material [8]], the polycrystalline samples of $La_3Ni_2O_{7-\delta}$ and $La_2PrNi_2O_{7-\delta}$ crystallize in the *Cmcm* orthorhombic structure; i.e., they represent the 2222 polymorph. Synchrotron powder diffraction data for $La_3Ni_2O_7$ reveal approximately 4% of $La_4Ni_3O_{10}$ impurity. Thermogravimetric analysis reveals $\delta = 0.01(1)$ and 0.04(1) for $La_3Ni_2O_{7-\delta}$ and $La_2PrNi_2O_{7-\delta}$, respectively, which indicates that the samples are nearly oxygen stoichiometric [Fig. 2(b); Fig. S4 of the Supplemental Material [8]]. The Rietveld refinement of the high-resolution neutron powder diffraction data further confirms full occupancy of the individual oxygen positions [Fig. 2(c)]. Hereafter, we will designate these samples as $La_3Ni_2O_7$ and $La_2PrNi_2O_7$.

Previously, in addition to the SDW, a second density wave (DW) transition was observed in the electrical transport data for undoped $La_3Ni_2O_7$ at $T \sim 130$ K and ambient pressure [18]. To check the possibility of long-range structural order, variable-temperature synchrotron x-ray diffraction and high-resolution NPD experiments were performed. Patterns collected above and below the DW transition (Fig. S6 of the Supplemental Material [8]) reveal no resolvable superlattice reflections or additional scattering, indicating that any long-range structural component is below the sensitivity limits of powder diffraction. Rietveld refinement confirms that the high-temperature *Cmcm* model remains robust at low temperatures, and we find no evidence for a $q = 0$ transition or significant Ni–O bond disproportionation (Table S1 of the Supplemental Material [8]).

However, the absence of detectable structural peaks in powder data does not preclude the existence of CDW physics. In many correlated oxides, the atomic displacements associated with CDW order are extremely small and easily obscured by the powder background. Indeed, recent single-crystal x-ray diffraction studies provide crucial insight into the charge order behavior of $La_3Ni_2O_7$, revealing two inequivalent Ni sites at room temperature due to a symmetry lowering from *Cmcm* to the chiral *Cm*2*m* space group [33]. Crucially, the reflections violating the *c*-glide plane are reported to be 4 orders of magnitude weaker than the principal Bragg reflections. Such subtle features are inherently inaccessible via powder diffraction, which explains the lack of a detectable structural signature in our measurements.

B. μSR characterization

Magnetic order has previously been observed in $La_3Ni_2O_7$ [18,34] and $La_2PrNi_2O_7$ [35] by means of μSR. Notably,

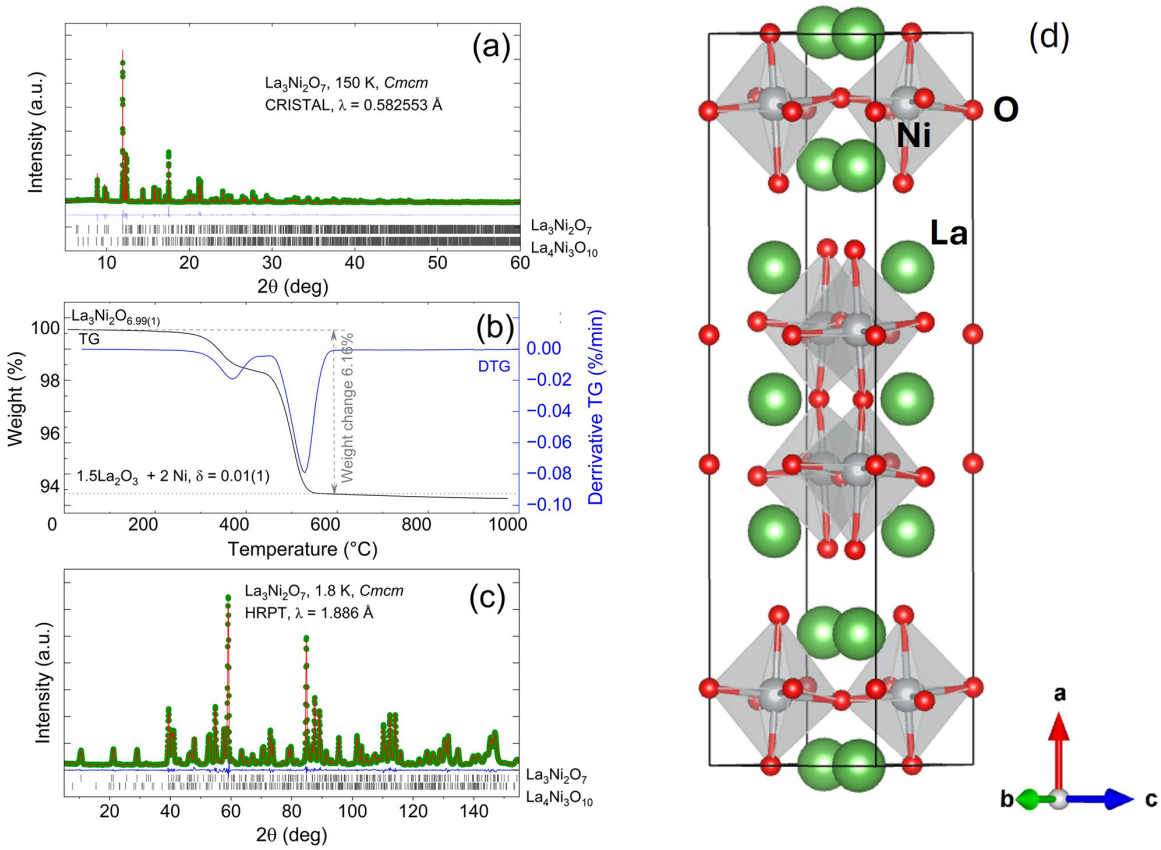

FIG. 2. X-ray and neutron powder diffraction refinement, thermogravimetric analysis, and crystal structure of $La_3Ni_2O_7$. Rietveld refinement of the high-resolution synchrotron x-ray [panel (a)] and high-resolution neutron [panel (c)] powder diffraction patterns for $La_3Ni_2O_7$. Green circles: observed data; red line: calculated pattern. The blue line represents the difference between measured and calculated data points. The vertical ticks indicate the positions of the Bragg reflections for the *Cmcm*-$La_3Ni_2O_7$ main phase and *Cmca*-$La_4Ni_3O_{10}$ impurity. (b) Hydrogen reduction thermogravimetric analysis for $La_3Ni_2O_7$: weight loss and derivative of the thermogravimetric (TG) curve (DTG). (d) Projection of the refined crystal structure for $La_3Ni_2O_7$. The structure is visualized using VESTA software [36].

the pressure-dependent μSR results for $La_2PrNi_2O_7$ reported in Ref. [35] were obtained from the same batch of samples investigated in the present study. To ensure consistency with these earlier findings, we performed additional μSR characterization on the two samples used for the neutron diffraction measurements reported here. The details of the μSR analysis are provided in the Supplemental Material [8], while the main conclusions are summarized below.

The weak-transverse-field (WTF) μSR measurements reveal bulk magnetism, with a magnetic volume fraction exceeding 95% at 80 K, below $T_N = 149.5$ K in both samples, as follows from Figs. 3(a)–3(d) and Fig. S5 of the Supplemental Material [8]. Characteristic zero-field (ZF) μSR spectra are presented in Figs. 3(e) and 3(f), and their Fourier transforms in panels (g) and (h) reveal five components. Three of these, fast-precessing, slow-precessing, and fast-relaxing signals (highlighted in blue), are consistent with previous reports [18,35]. In addition, two further peaks at internal fields $B_{\text{int}} \simeq 110$ and 40 mT (indicated by dashed lines) were not reported earlier. We note that the spectra in Figs. 3(e) and 3(f) were collected with substantially higher muon statistics than in Refs. [18,35], enabling the detection of these additional features. Based on our analysis, these extra components can be attributed to either the $La_4Ni_3O_{10}$ phase or 1313 polymorph [37], which have similar μSR frequencies. Indeed, approximately 4% of $La_4Ni_3O_{10}$ phase has been observed in the synchrotron diffraction experiment. Although this content is slightly lower than that evident from μSR, we can argue that this discrepancy can be attributed to the difference in the length scales probed. While diffraction methods require well-defined long-range structural order, μSR signal can be generated by clusters of several lattice spacings; i.e., it is also sensitive to local features, such as stacking faults or interfacial boundaries, which are prevalent in layered RP nickelates [5]. A detailed discussion of the role of the stacking faults and homologs/polymorphs is provided in Supplemental Material [8].

The fast- and slow-precessing components at 145 mT/10 mT for $La_3Ni_2O_7$ and 143 mT/14 mT for $La_2PrNi_2O_7$ are associated with static magnetic SDWs in these materials. Pr substitution has only a marginal effect on the μSR response. Previously, based on dipole-field simulations, we identified features of the magnetic order consistent with the observed μSR signals [18]: (1) The symmetric shape of the peaks in the field distribution is characteristic of a commensurate, rather than incommensurate, order, and (2) the presence of low-field (10 and 14 mT) and high-field (145 and 143 mT) peaks is ascribed to two symmetry-inequivalent magnetic Ni

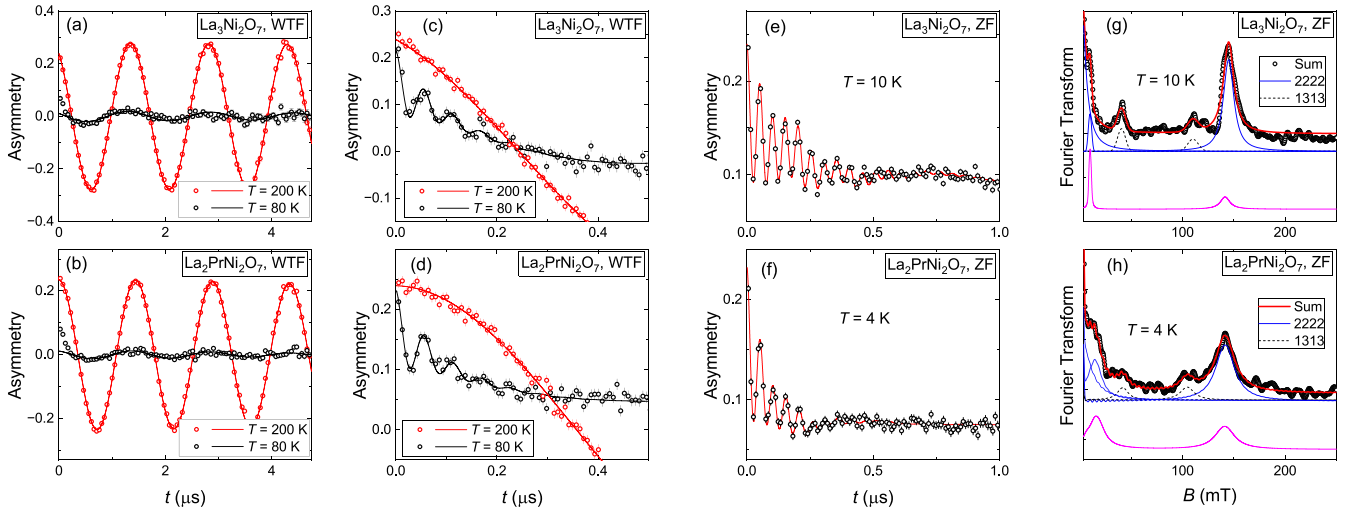

FIG. 3. Magnetic response of $La_3Ni_2O_7$ and $La_2PrNi_2O_7$ probed by μSR. (a), (b) μSR time spectra collected in weak-transverse-field experiments ($B_{WTF} = 5$ mT) above ($T = 200$ K) and below ($T = 80$ K) the SDW ordering temperature T_N. (c), (d) The extended part of WTF-μSR data presented in panels (a) and (b). (e), (f) Zero-field μSR time spectra measured at low temperatures. (g), (h) Fourier transforms of the data presented in panels (e) and (f). The solid lines are fits by using Eqs. (1)–(4) from the Methods section (see text for details). The pink lines are results of the dipolar-field calculations.

sites. These conclusions will be used for the analysis of the elastic magnetic neutron scattering data.

C. Observation of magnetic neutron scattering

For $La_3Ni_2O_7$, the neutron powder diffraction pattern collected at DMC at $T = 1.5$ K (after subtracting the $T = 200$ K data) reveals five additional reflections at $2\theta = 26.0°$, 29.7°, 34.0°, 48.9°, and 54.8° [Figs. 4(a) and 4(b)]. Although weak, these reflections can still be traced in the $T = 130$ K pattern [Fig. 4(c)], whereas they are completely gone at $T = 150$ K [Fig. 4(d)], indicating a transition in this temperature range. These reflections are not broadened, and their amplitude is on the order of 0.1% relative to the main nuclear reflections.

As follows from a comparison of the difference neutron diffraction patterns for the pristine and Pr-substituted $La_3Ni_2O_7$ [Fig. 4(b) versus Fig. 5(b)], the latter shows only one reflection at ∼29.7° in the range between 25° and 35°. Following the findings of preceding μSR investigations [18], which suggested commensurate SDW order, all of the observed reflections in $La_2PrNi_2O_7$ can be indexed using a commensurate propagation vector $q_{1,t} = (\frac{1}{4}, \frac{1}{4}, 0)$ relative to the quasitetragonal (*I4/mmm*; Fig. S2 of the Supplemental Material [8]) subcell, which transforms to $q_1 = (0, \frac{1}{2}, 0)$ in the orthorhombic *Cmcm* basis ($a = 20.24$ Å, $b = 5.43$ Å, $c = 5.34$ Å). This is consistent with the wave vector deduced from previous resonant x-ray scattering measurements [13,20]. Although the undoped $La_3Ni_2O_7$ exhibits notably more reflections emerging upon cooling, some of them [for instance, $2\theta = 29.7°$; Fig. 4(b)] can still be indexed with q_1, whereas others (for instance, $2\theta = 26.0°$ and 34.0°) can be indexed with $q_2 = (\frac{1}{2}, \frac{1}{2}, 0)$ [in *I4/mmm* setting, $q_{2,t} = (\frac{1}{4}, \frac{1}{4}, \frac{1}{2})$], which is not symmetry equivalent to q_1.

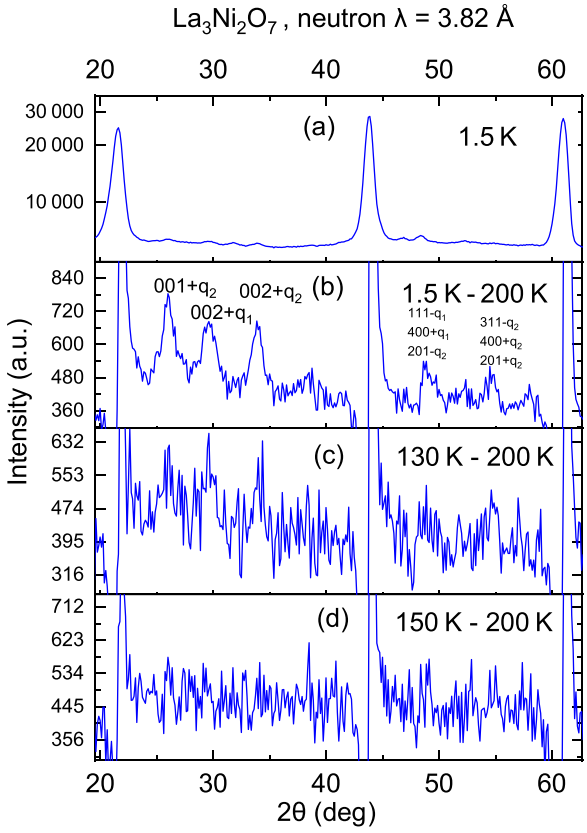

FIG. 4. Magnetic neutron scattering in $La_3Ni_2O_7$. Raw neutron powder diffraction pattern for $La_3Ni_2O_7$ at (a) $T = 1.5$ K (y axis is in logarithmic scale) and difference neutron powder diffraction patterns ($T = 200$ K) for $T = 1.5$ K [panel (b)], $T = 130$ K [panel (c)], and $T = 150$ K [panel (d)]. The indexes of magnetic reflections in panel (b) are indicated according to the indexing described in the text.

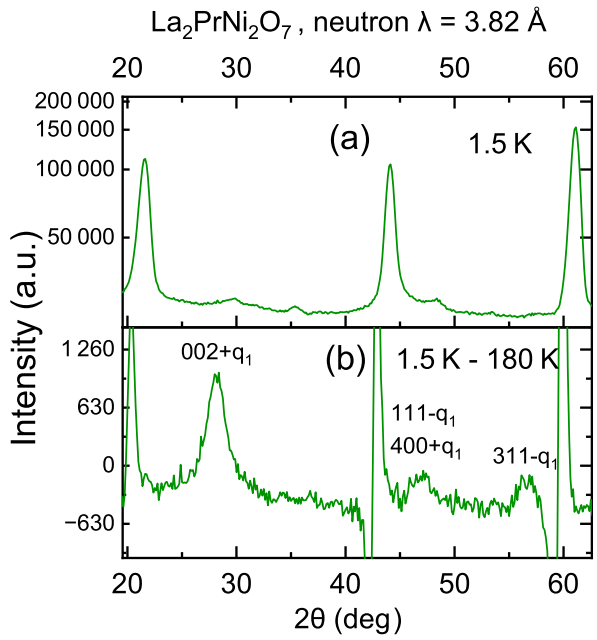

FIG. 5. Magnetic neutron scattering in $La_2PrNi_2O_7$. Raw neutron powder diffraction pattern at (a) $T = 1.5$ K (y axis is in logarithmic scale) and (b) difference 1.5–180 K pattern for $La_2PrNi_2O_7$. The indexes of magnetic reflections in panel (b) are indicated according to the indexing described in the text.

The neutron intensities of the reflections emerging at low temperatures decrease with increasing 2θ angle, indicating that these reflections follow the magnetic rather than the nuclear form factor [38]. Furthermore, as outlined in the previous section, no additional reflections were detected in synchrotron diffraction data, implying significantly different neutron and x-ray scattering cross sections leading to those neutron reflections. Magnetism in $La_4Ni_3O_{10}$ manifests in neutron powder diffraction as a single broad peak spanning 25°–32° in 2θ [39].

Additionally, the two propagation vectors (q_1 and q_2) observed in the undoped sample are not related by the expected relation $q_{CDW} = 2q_{SDW}$, as is the case for $La_4Ni_3O_{10}$ [32]. Importantly, in $La_4Ni_3O_{10}$ the nuclear superstructure associated with the structural component of the CDW is also not visible in the neutron data. Combining the above-mentioned facts, it is to conclude that the reflections observed in the NPD (Fig. 4) are attributed to magnetic order in $La_3Ni_2O_7$ phase.

D. Representation and magnetic symmetry analysis

Symmetry-allowed models of spin structures were constructed and tested against the neutron data using the representation and magnetic symmetry routine implemented in JANA2006/JANA2020 [40,41] and isodistort [42,43]. Table S2 of the Supplemental Material [8] provides possible maximal magnetic subgroups of the parent *Cmcm* space group compatible with q_1 (*DT* point of Brillouin zone) and q_2 (*S* point of Brillouin zone) [44–47]. The *DT* point yields four irreducible representations (irreps), each giving rise to two magnetic space groups (MSGs). Testing these irreps against the magnetic intensities observed for the $La_2PrNi_2O_7$ sample shows that only one, namely, *mDT1*, is compatible with the experimental data, as evidenced by the R values summarized in Table S2 of the Supplemental Material [8]. This irrep also reproduces the q_1 magnetic intensities observed in $La_3Ni_2O_7$ equally well. Among the two possible solutions, $Pmma.1'_c[Pmma]$ corresponds to a constant-moment structure with all Ni sites magnetically equivalent, whereas $Pmmn.1'_c[Pmmn]$ represents an SDW state with two distinct, refinable moment amplitudes on the Ni atoms. Since our μSR measurements favor the latter scenario, we conclude that the $Pmmn.1'_c[Pmmn]$ model uniquely accounts for both the neutron diffraction and μSR results.

TABLE I. Details of magnetic q_1 and q_2 structures in $La_3Ni_2O_7$: magnetic space groups [48,49], cell parameters, basis transformation from the parent nuclear *Cmcm* cell to the magnetic cell, atomic positions, and corresponding magnetic moments. Only magnetic Ni atoms are provided.

Atom	x	y	z	M_x	M_y	M_z
			$\boldsymbol{q_1}$ model			
			$Pmmn.1'_c[Pmmn]$ (UNI No. 59.413 [49])			
			$a = 20.49$ Å, $b = 5.39$ Å, $c = 10.92$ Å			
			Basis = {(1, 0, 0), (0, 0, 1), (0, −2, 0)}			
Ni1	0.847	0.25	0.749	0	0.87(3)	0
Ni2	0.347	0.25	0.999	0	0.16(4)	0
			$\boldsymbol{q_2}$ model			
			$P2_1/m.1'_a[P2_1/m]$ (UNI No. 11.55 [49])			
			$a = 10.92$ Å, $b = 5.39$ Å, $c = 21.21$ Å, $\beta = 104.9°$			
			Basis = {(0, 2, 0), (0, 0, 1), (1, −1, 0)}			
Ni1	−0.075	0.25	0.597	0	0.87(3)	0
Ni2	−0.075	0.25	0.097	0	0.16(4)	0
Ni3	0.327	0.25	0.403	0	0.16(4)	0
Ni4	0.327	0.25	−0.097	0	0.87(3)	0

A similar consideration allows us to conclude that for the *S* point, out of four possible irreps—each generating three MSGs—the *mS*1+ and *mS*2− are the plausible candidates (Table S2 of the Supplemental Material [8]). The sets of solutions generated by these two irreps are symmetrically identical but differ by an origin shift relative to the parent *Cmcm* structure. Without loss of generality, we therefore consider only the *mS*1+ solutions. Analogous to the case of q_1, only the $P2_1/m.1'_a[P2_1/m]$ model produces an amplitude-modulated spin density wave and was thus selected as the final solution. Since the latter solution is monoclinic, we checked the possibility of distortion in the parent nuclear structure, but did not find convincing evidence for that.

The derived models, along with the corresponding Rietveld plots, are presented in Fig. 6. The model derived for the q_1 in the case of $La_2PrNi_2O_7$ fits q_1 intensities in $La_3Ni_2O_7$ equally well. The details of the magnetic structure for q_1 and q_2 are summarized in Table I.

For both q_1 and q_2 vectors, a single magnetic Ni layer is formed by alternating high- and low-moment stripes. From the comparison of the stacking sequences along the c axis [Figs. 6(d) and 6(e)], we can conclude that q_1 and q_2 correspond to two distinct stacking magnetic polymorphs. Assuming that the whole volume of $La_2PrNi_2O_7$ sample is occupied by the 2222 phase, and using the scale factor

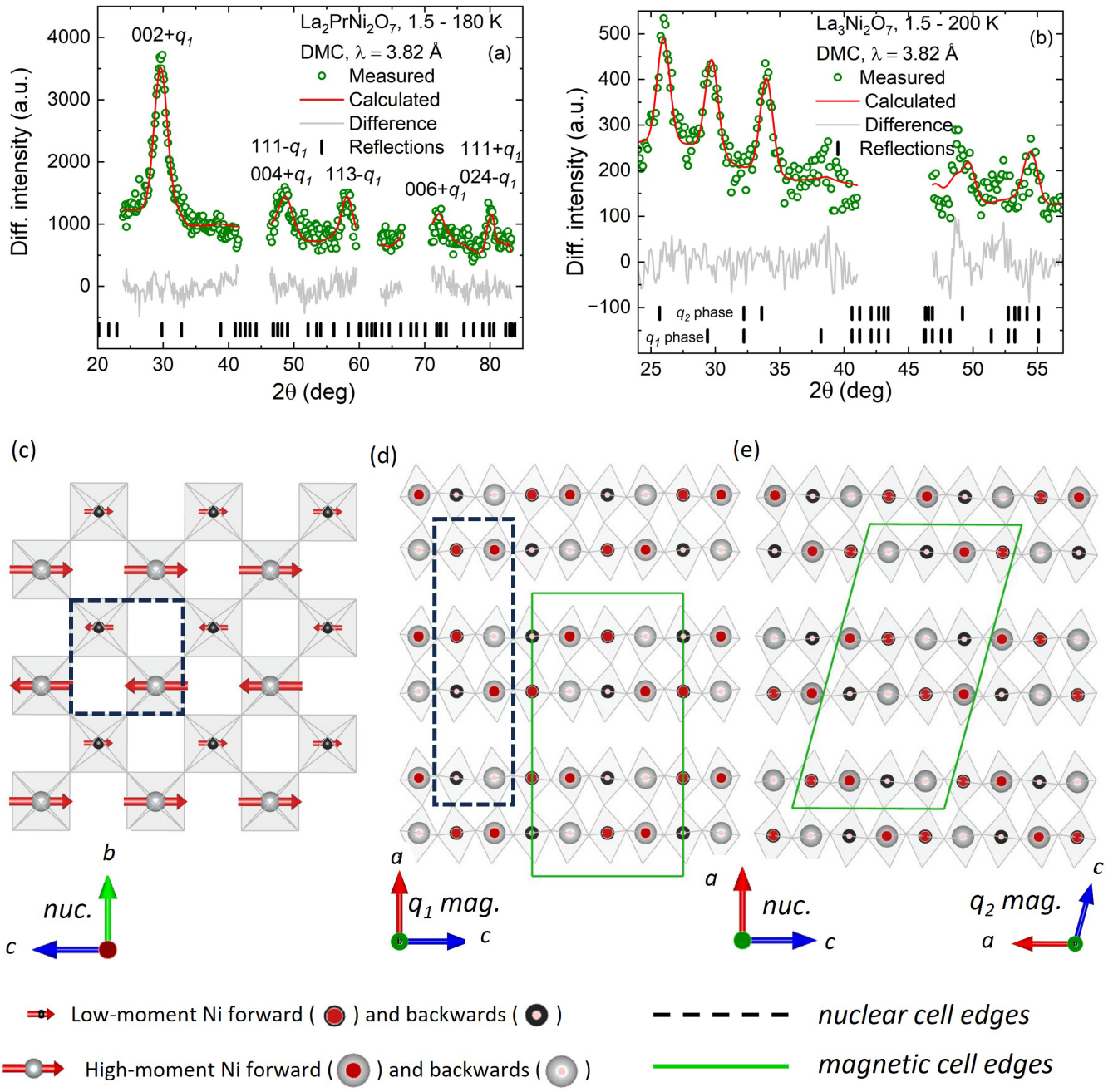

FIG. 6. Neutron powder diffraction magnetic responses and magnetic models of $La_3Ni_2O_7$ and $La_2PrNi_2O_7$. Rietveld refinement plots on difference neutron powder diffraction patterns for 1.5–180 K $La_2PrNi_2O_7$ [panel (a)] and 1.5–200 K $La_3Ni_2O_7$ [panel (b)]. The gaps are at the positions of the principal nuclear reflections. (c) Projections of arrangement of magnetic moments for a single Ni grid (view perpendicular to the single Ni layer) for both q_1 and q_2 models. Axis is given relative to the parent nuclear cell. The magnetic moments on low- and high-moment sites are not to the scale. Stacking sequence of single Ni grids along the c axis for q_1 [panel (d)] and q_2 [panel (e)]. The axes for panels (d) and (e) relative to the magnetic cells are given on the left and right sides, respectively (Table I); the axis for the parent nuclear cell is given in the middle. Magnetic unit cells corresponding to q_1 and q_2 are outlined in green in panels (d) and (e); the parent nuclear cell is outlined in gray dashed line in panels (c) and (d). Three-dimensional views of magnetic unit cells are provided in Fig. S9 of the Supplemental Material [8]. Panels (c), (d), and (e) were visualized using VESTA software [36].

derived in this way, the values of the magnetic moment for the q_1 model in the $La_2PrNi_2O_7$ on high- and low-moment sites are $0.85(15)\mu_B$ and $0.15(5)\mu_B$. With this assumption applied to $La_3Ni_2O_7$, considering that the sample contains two magnetic polymorphs (q_1 and q_2) as two independent magnetic phases in 25(1)% versus 75(1)% ratio and constraining the values of low- and high-moment sites in q_1 and q_2 models, the derived magnetic moments are $0.87(3)\mu_B$ and $0.16(4)\mu_B$.

The final refinement of the $La_3Ni_2O_7$ is based on a total of 14 magnetic reflections, 5 of which can be considered as visible (above 3σ); refined are three independent parameters:

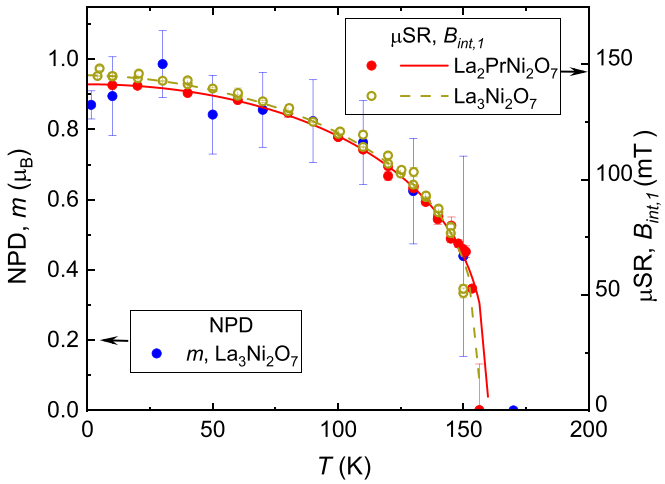

FIG. 7. Comparison of NPD and μSR magnetic responses. Comparison of the temperature dependence of magnetic moment (m, μ_B) for the high-moment site in $La_3Ni_2O_7$ derived from NPD data according to the models for q_1 and q_2 with the temperature evolution of fast precession component of the internal field ($B_{\text{int},1}$, mT) derived from μSR measurements for $La_3Ni_2O_7$ (dashed line) and $La_2PrNi_2O_7$ (solid line). The error bars for the neutron and muon data are statistical.

two components of magnetic moments (low and high Ni moments) and phase fraction. The scale factor was derived from the nuclear refinement and fixed for the magnetic one. Note that the provided error bars are purely statistical from the least-squares refinement; they do not account for errors introduced by the background correction. The latter is set up manually and not adjusted during the fitting. Hence, the physically realistic error bars should be larger.

E. Comparison of NPD and μSR magnetic responses: Consistent trends

In order to test that the observed magnetic scattering at low temperature (below $T \approx 150$ K) is common with SDW observed by μSR experiments, the order parameter evolution as the function of temperature is presented in Fig. 7, superimposing the results of both NPD ($La_3Ni_2O_7$) and μSR ($La_{3-x}Pr_xNi_2O_7$, $x = 0$ and 1). The neutron and muon data show a clear agreement, although the error bars for neutron-derived magnetic moments are relatively large compared to the magnetic order parameter as observed by μSR.

To further validate the consistency of neutron and μSR, we have performed simulations of the dipole field at the DFT-calculated muon site, following the approach in Ref. [18]. Both $La_3Ni_2O_7$ and $La_2PrNi_2O_7$ exhibit qualitatively similar ZF-μSR responses [Figs. 3(e)–3(h)], suggesting the necessity for some sites to have close-to-zero magnetic moment to explain the low-field muon site.

Dipole-field simulations for the $\boldsymbol{q_1}$ model [Figs. 6(c) and 6(d)] suggest that this spin structure is compatible with the μSR data for $La_2PrNi_2O_7$ when the high- and low-moment sites carry magnetic moments of $0.655\mu_B$ and $0.075\mu_B$, respectively. With these values, the simulations yield internal fields of approximately 141 and 14 mT, in excellent agreement with the experimental data ($B_{\text{int},1} \simeq 143$ mT and $B_{\text{int},2} \simeq 14$ mT). The pink line in Fig. 3(g) represents the simulated field distribution. From the experimental results, we expect about 82% and 18% of the muons to stop at the high- and low-field sites, respectively, whereas the simulations suggest equal occupancy of both sites. In the simulation, a perfectly ordered infinite magnetic structure is assumed; in reality, the finite magnetic correlation length modifies the fraction of muons occupying each site. The discrepancy between the simulated and experimental results may therefore indicate that the correlation length is relatively short in at least one crystallographic direction in $La_2PrNi_2O_7$. Indeed, previous diffraction studies on $La_4Ni_3O_{10}$ have shown that both magnetic and atomic superstructures exhibit extended correlation lengths exceeding 100 Å within the ab plane, whereas the coherence along the intergrowth direction is poor and does not extend beyond a single unit-cell period [32]. This behavior is attributed to the formation of stacking faults during intergrowth.

We now turn to the undoped $La_3Ni_2O_7$, which, unlike the Pr substituted sample, shows magnetic neutron scattering at two vectors, q_1 and q_2, with q_2 being dominant. The q_2 model provided in Figs. 6(c) and 6(e) is compatible with the muon data when the high and low moments are $0.66\mu_B$ and $0.05\mu_B$, respectively, with an equal fraction of the muons sensitive to an internal field of around 10 or 141 mT. The values of the internal field are in agreement with the results presented in Fig. 3(h) and in Ref. [18]. Once again, experimentally fewer muons stop in the low-field site compared to the simulation, which again likely reflects a relatively short correlation length along the out-of-plane direction.

The differences between the values of magnetic moments derived from NPD and μSR are $\sim 0.1\mu_B$ and $\sim 0.2\mu_B$ for low- and high-moment sites, e.g., mostly fall close to or slightly above the error bars calculated from the Rietveld fit of the neutron data. This further validates the models proposed from the representation and magnetic symmetry analysis. Still, the muon values are systematically lower than the neutron ones. We see several reasons for this discrepancy. First, as mentioned above, the magnetic signal seen by neutrons is rather weak, which causes an arbitrary process of background correction to introduce sizable uncertainties. Another source of systematic error is the presence of 10%–15% of 1313 polymorph confined to interface boundaries or crystallized $La_4Ni_3O_{10}$, as evident from the μSR data. In addition, due to the itinerant nature of magnetism in the metallic oxygen-stoichiometric $La_{2-x}Pr_xNi_2O_7$ [50], as evidenced by the reduced values of the ordered magnetic moments, the magnetic neutron form factor is expected to be more complex than in the localized-moment case. The estimation of the magnetic form factor is, however, beyond the scope of the present work. Overall, we judge the representation and magnetic symmetry analysis done on neutron data to directly yield the spin arrangement, whereas μSR is more faithful in determining the absolute values of magnetic moments.

III. CONCLUSIONS AND OUTLOOK

Previous neutron studies of $La_3Ni_2O_{7-\delta}$ revealed no elastic scattering (Bragg diffraction) associated with long-range

magnetic order [4,29,30], whereas resonant x-ray scattering [13,20] and μSR [18,22] experiments, in line with macroscopic property measurements, show the presence of SDW. The lack of magnetic diffraction in neutron experiments was ascribed either to a small magnetic moment or to the short-range character of the order [18,29]. Contrary to that, the neutron data presented in our report unambiguously indicate the long-range magnetic order evident from the magnetic Bragg peaks (Figs. 4 and 6), associated with a magnetic moment of $\sim 0.66 \mu_B$ on half of the Ni atoms.

This apparent contradiction between the previous reports and our current work can be ascribed to several factors related to the sample and the neutron experiment setup. Our samples are close to ideal stoichiometry. Theory [51] and μSR [34] studies suggested oxygen stoichiometry as the crucial factor defining the ground-state magnetic order in the title material. Additionally, our measurements were performed on large samples ($\sim$10 g) using a recently upgraded high-flux neutron diffractometer dedicated to studying small magnetic moment systems [52].

The direct observation of the magnetic neutron scattering enabled the first unambiguous determination of the nature of the SDW state in bilayer nickelates, also consistent with μSR data, ^{139}La-NQR results [53], and recent theory studies [54,55]. The detailed discussion on possible origin of magnetic polymorphism and its interplay with superconductivity is provided in the Supplemental Material [8,56–60]. While previous μSR studies indicate that the SDW transition temperature increases under applied pressure [18], its precise relationship with the emergence of superconductivity remains a pivotal question.

Notably, in a separate study, we employed the oxygen isotope effect (OIE) to investigate the CDW and SDW transition temperatures in $La_3Ni_2O_7$ and $La_4Ni_3O_{10}$ [61]. The OIE provides a powerful means to disentangle purely electronic effects from those driven by phonons. In contrast to the trilayer compound, where CDW and SDW transitions appear to be coupled, $La_3Ni_2O_7$ exhibits an SDW transition that is nearly insensitive to oxygen isotope substitution. This effective decoupling of phononic and electronic subsystems points to a predominantly electronic origin of the SDW in the bilayer system. Future high-pressure neutron diffraction experiments performed closer to the superconducting dome, together with detailed structural investigations, will be crucial for elucidating the interplay between magnetic and structural order present in the ground state and the emergence of pressure-induced superconductivity in $La_3Ni_2O_7$. Such studies will help clarify whether the SDW or CDW constitutes a competing instability or a possible precursor to unconventional superconductivity—an issue central to understanding the physics and the primary mechanism of superconductivity in Ruddlesden-Popper nickelates [28,61].

IV. METHODS

A. Sample preparation

The samples studied in this work were prepared via a solid-state reaction from NiO (4N8, Alfa Aesar), La_2O_3 (5N, Sigma-Aldrich), and Pr_6O_{11} (5N, Sigma-Aldrich) through a mechanochemically assisted process similar to that described previously [18]. Stoichiometric mixtures of the calcinated oxides were ball-milled (800 rpm, 5 min grinding, 5 min pause, 20 cycles), pressed into pellets, and annealed in oxygen flow for 100 h at 1250 °C ($La_3Ni_2O_7$) or for 70 h at 1100 °C ($La_2PrNi_2O_7$) with intermediate grindings and a postannealing stage (24 h/500 °C). For $La_2PrNi_2O_7$, the annealing temperature was chosen according to Ref. [5].

B. X-ray powder diffraction

Samples' purity was checked, and data for structure refinement were collected at room temperature using a bruker AXS D8 ADVANCE diffractometer (Cu Kα radiation). Variable-temperature synchrotron powder diffraction datasets were collected at the CRISTAL beamline (Soleil Synchrotron) using $\lambda = 0.582\ 553$ Å radiation. A Rietveld analysis of the obtained x-ray diffraction pattern at 150 K was performed utilizing the jana software [41]. This analysis yielded the following unit cell parameters of the orthorhombic structure (*Cmcm*, Space Group No. 63): $a = 20.4970(1)$ Å; $b = 5.447\ 81(3)$ Å; $c = 5.378\ 35(3)$ Å. The reliability factors of the fit were as follows: $R_p = 5.7$; $R_{WP} = 7.6$; GOF = 9.7; and $R_I = 4.1$.

C. Oxygen content determination

The oxygen content in the $La_{3-x}Pr_xNi_2O_{7-\delta}$ ($x = 0$ and 1) samples was determined by hydrogen-reduction thermogravimetric analysis (TGA). A NETZSCH STA 449F1 simultaneous thermal analyzer was used for the TGA experiments. The initial sample masses were 144.04 and 83.29 mg for $x = 0$ and 1, respectively. The gas utilized was a mixture of 5 vol % hydrogen (Messer SchweizAG, 5N) in helium (PanGas, 6N), with a flow rate of 70 ml/min. The sample was heated from room temperature to 1000 °C at a rate of 1 °C/min and subsequently cooled to room temperature. In order to minimize buoyancy effects and friction forces resulting from the vertical gas flow, and thereby ensure an accurate estimation of weight changes, a baseline measurement was performed under identical conditions before measuring the actual samples. The total weight loss can be attributed to the reduction of $La_{3-x}Pr_xNi_2O_{7-\delta}$ to metallic nickel (Ni) and R_2O_3 (R = La or Pr). The residual weight was estimated at a temperature corresponding to the reaction termination (T_f), determined from the final plateau in the first derivative of the TG weight-loss curve.

D. Neutron powder diffraction

High-intensity NPD datasets were collected on the cold-neutron powder diffractometer DMC [52,62] with 3.82 Å neutrons and high-resolution NPD dataset at the thermal neutron HRPT diffractometer [63] with 1.89 Å neutrons, both located at Paul Scherrer Institute. $\sim$10 g of $La_3Ni_2O_7$ and $\sim$11 g of $La_2PrNi_2O_7$ samples were loaded into V-cans, placed in an Orange He cryostat, and measured down to the base temperature of approximately 1.5–1.8 K. Analysis of the diffraction datasets, including representation and magnetic symmetry, was performed using JANA2006/JANA2020 software according to the standard mathematical approach for

powder diffraction data (pseudo-Voigt profile function and manual background) as described in Refs. [40,41]. The group-subgroup relations were analyzed using isordistort [42,43] and k-subgroupsmag software of the Bilbao Crystallographic Server [44,45].

E. Muon-spin rotation/relaxation experiments

Zero-field and weak-transverse-field μSR experiments were carried out at the Paul Scherrer Institute, Switzerland. Experiments were performed at the $\pi E3$ beamline using GPS [64] and FLAME [65] muon spectrometers. The μSR data were analyzed using the MUSRFIT software package [66].

F. Fits of WTF- and ZF-μSR data

The fit to the experimental WTF- and ZF-μSR data was performed using the following functional form:

$$A(t) = A_0\,P(t) = A_0[f_m\,P_m(t) + (1 - f_m)\,P_{\rm nm}(t)]. \qquad (1)$$

Here, A_0 is the initial asymmetry and $P(t)$ represents the time evolution of the muon-spin polarization. The polarization function $P(t)$ is further divided into the magnetic and nonmagnetic contributions with weights f_m and $1 - f_m$, respectively. The magnetic part is caused by the appearance of SDW order and is described as

$$P_m(t) = \frac{2}{3}\sum_i f_i e^{-\lambda_{{\rm T},i}t}\cos(\gamma_\mu B_{{\rm int},i}t) + \frac{1}{3}e^{-\lambda_{\rm L}t}. \qquad (2)$$

Here, $\gamma_\mu = 851.616\,{\rm MHz/T}$ is the muon gyromagnetic ratio, λ's denote the exponential relaxation rates, and f_i is the volume fraction of the ith magnetic component ($\sum_i f_i = 1$). The coefficients $2/3$ and $1/3$ account for powder averaging, where $2/3$ of the muon spins precess in internal fields perpendicular (transversal, T) to the field direction and $1/3$ remain parallel (longitudinal, L) to $B_{{\rm int},i}$.

The nonmagnetic part in ZF experiments is described by the Gaussian Kubo-Toyabe (GKT) function [67], which can be written as

$$P^{\rm ZF}_{\rm nm}(t) = \tfrac{2}{3}\big(1 - \sigma^2_{\rm GKT}t^2\big)e^{\sigma^2_{\rm GKT}t^2/2} + \tfrac{1}{3}. \qquad (3)$$

Here, $\sigma_{\rm GKT}$ is the relaxation rate. This function is typically used to describe the nuclear moment contribution in ZF-μSR experiments.

In WTF experiments, the nonmagnetic part is described by a simple cosine oscillation with exponential relaxation:

$$P^{\rm WTF}_{\rm nm}(t) = e^{-\lambda t}\ \cos(\gamma_\mu B_{\rm WTF}\,t + \phi). \qquad (4)$$

Here, λ is the exponential relaxation rate, $B_{\rm WTF}$ is the externally applied weak transverse field, and ϕ is the initial phase of the muon-spin ensemble.

In the present study, the WTF-μSR data are analyzed in two modes: the "long" and the "short" time-window modes. In the "long time-window" case, the magnetic term in Eq. (1) was neglected, and the data are analyzed using the nonmagnetic term [Eq. (4)] only. To avoid the influence of SDW magnetism, fits started after $\sim$0.3 μs. This approach allows tracking the temperature dependence of the magnetic fraction f_m. The short time-window mode considers data up to 1 μs only, and the analysis was performed using both the magnetic and nonmagnetic terms of Eq. (1). This makes it possible to follow the evolution of the strongest component of the internal field ($B_{{\rm int},1}$ in our case).

G. The dipole-field calculations

The dipole-field calculations were performed assuming the same muon site as reported in Ref. [18] for both $La_3Ni_2O_7$ and $La_2PrNi_2O_7$, and utilized the muesr code [68].

Note added. During the revision of this article, a recent preprint reporting neutron diffraction and inelastic neutron scattering measurements on single crystals of $La_3Ni_2O_7$ appeared [69]. The authors report magnetic reflections associated with the propagation vector q_2, but not q_1. We consider these results as (1) an independent confirmation of our findings, (2) evidence for pronounced sample dependence within the $La_3Ni_2O_7$ family, and (3) support for the single-q/multiphase scenario over the multi-q scenario.

ACKNOWLEDGMENTS

Z.G. acknowledges support from the Swiss National Science Foundation (SNSF) through SNSF Starting Grant (No. TMSGI2_211750). This work is based on experiments performed at the Swiss Spallation Neutron Source SINQ and the Swiss Muon Source SμS, Paul Scherrer Institute, Villigen, Switzerland. I.P. acknowledges support from Paul Scherrer Institute Research Grant No. 2021 01346. D.J.G. acknowledges support from the Swiss National Science Foundation (SNSF) through Grant No. 200021E_238113. P. F.-L. acknowledges support from the French National Research Agency (ANR) SUNSHINE No. ANR-25-CE30-7264 and SUPERNICKEL No. ANR-21-CE30-0041-04. The authors acknowledge Professor George Sawatzky for valuable discussion of the results.

I.P., R.K., and D.J.G. conceived and supervised the project; I.P. and D.J.G. prepared the samples and performed their x-ray and TG characterization; I.P., L.K., V.P., and S.H.M. performed neutron diffraction experiments and analyzed the data; P.F.-L. performed synchrotron diffraction experiments; R.K., J.J.K., H.L., Z.G., and T.J.H. performed μSR experiments and analyzed the data; I.P., R.K., T.J.H., and D.J.G. wrote the manuscript with contributions from all co-authors.

DATA AVAILABILITY

The data that support the findings of this article are not publicly available upon publication because it is not technically feasible and/or the cost of preparing, depositing, and hosting the data would be prohibitive within the terms of this research project. The data are available from the authors upon reasonable request.

[1] M. Wang, H.-H. Wen, T. Wu, D.-X. Yao, and T. Xiang, Normal and superconducting properties of $La_3Ni_2O_7$, Chin. Phys. Lett. **41**, 077402 (2024).

[2] H. Sun, M. Huo, X. Hu, J. Li, Z. Liu, Y. Han, L. Tang, Z. Mao, P. Yang, B. Wang, *et al.*, Signatures of superconductivity near 80 K in a nickelate under high pressure, Nature (London) **621**, 493 (2023).

[3] J. Hou, P.-T. Yang, Z.-Y. Liu, J.-Y. Li, P.-F. Shan, L. Ma, G. Wang, N.-N. Wang, H.-Z. Guo, J.-P. Sun, Y. Uwatoko, M. Wang, G.-M. Zhang, B.-S. Wang, and J.-G. Cheng, Emergence of high-temperature superconducting phase in pressurized $La_3Ni_2O_7$ crystals, Chin. Phys. Lett. **40**, 117302 (2023).

[4] G. Wang, N. N. Wang, X. L. Shen, J. Hou, L. Ma, L. F. Shi, Z. A. Ren, Y. D. Gu, H. M. Ma, P. T. Yang, Z. Y. Liu, H. Z. Guo, J. P. Sun, G. M. Zhang, S. Calder, J.-Q. Yan, B. S. Wang, Y. Uwatoko, and J.-G. Cheng, Pressure-induced superconductivity in polycrystalline $La_3Ni_2O_{7-\delta}$, Phys. Rev. X **14**, 011040 (2024).

[5] N. Wang, G. Wang, X. Shen, J. Hou, J. Luo, X. Ma, H. Yang, L. Shi, J. Dou, J. Feng, *et al.*, Bulk high-temperature superconductivity in pressurized tetragonal $La_2PrNi_2O_7$, Nature (London) **634**, 579 (2024).

[6] X. Huang, H. Zhang, J. Li, M. Huo, J. Chen, Z. Qiu, P. Ma, C. Huang, H. Sun, and M. Wang, Signature of superconductivity in pressurized trilayer-nickelate $Pr_4Ni_3O_{10-\delta}$, Chin. Phys. Lett. **41**, 127403 (2024).

[7] H. Sakakibara, M. Ochi, H. Nagata, Y. Ueki, H. Sakurai, R. Matsumoto, K. Terashima, K. Hirose, H. Ohta, M. Kato, *et al.*, Theoretical analysis on the possibility of superconductivity in the trilayer Ruddlesden–Popper nickelate $La_4Ni_3O_{10}$ under pressure and its experimental examination: Comparison with $La_3Ni_2O_7$, Phys. Rev. B **109**, 144511 (2024).

[8] See Supplemental Material at http://link.aps.org/supplemental/10.1103/rw8k-tng5 for the details on μSR characterization.

[9] V. I. Anisimov, D. Bukhvalov, and T. M. Rice, Electronic structure of possible nickelate analogs to the cuprates, Phys. Rev. B **59**, 7901 (1999).

[10] H. Wang, L. Chen, A. Rutherford, H. Zhou, and W. Xie, Long-range structural order in a hidden phase of Ruddlesden–Popper bilayer nickelate $La_3Ni_2O_7$, Inorg. Chem. **63**, 5020 (2024).

[11] X. Chen, J. Zhang, A. S. Thind, S. Sharma, H. LaBollita, G. Peterson, H. Zheng, D. P. Phelan, A. S. Botana, R. F. Klie, and J. F. Mitchell, Polymorphism in the Ruddlesden–Popper nickelate $La_3Ni_2O_7$: Discovery of a hidden phase with distinctive layer stacking, J. Am. Chem. Soc. **146**, 3640 (2024).

[12] P. Puphal, P. Reiss, N. Enderlein, Y.-M. Wu, G. Khaliullin, V. Sundaramurthy, T. Priessnitz, M. Knauft, A. Suthar, L. Richter, M. Isobe, P. A. van Aken, H. Takagi, B. Keimer, Y. E. Suyolcu, B. Wehinger, P. Hansmann, and M. Hepting, Unconventional crystal structure of the high-pressure superconductor $La_3Ni_2O_7$, Phys. Rev. Lett. **133**, 146002 (2024).

[13] X. Chen, J. Choi, Z. Jiang, J. Mei, K. Jiang, J. Li, S. Agrestini, M. Garcia-Fernandez, H. Sun, X. Huang, D. Shen, M. Wang, J. Hu, Y. Lu, K.-J. Zhou, and D. Feng, Electronic and magnetic excitations in $La_3Ni_2O_7$, Nat. Commun. **15**, 9597 (2024).

[14] L. Wang, Y. Li, S.-Y. Xie, F. Liu, H. Sun, C. Huang, Y. Gao, T. Nakagawa, B. Fu, B. Dong, Z. Cao, R. Yu, S. I. Kawaguchi, H. Kadobayashi, M. Wang, C. Jin, H.-K. Mao, and H. Liu, Structure responsible for the superconducting state in $La_3Ni_2O_7$ at high-pressure and low-temperature conditions, J. Am. Chem. Soc. **146**, 7506 (2024).

[15] Y. Zhang, D. Su, Y. Huang, Z. Shan, H. Sun, M. Huo, K. Ye, J. Zhang, Z. Yang, Y. Xu, *et al.*, High-temperature superconductivity with zero resistance and strange-metal behaviour in $La_3Ni_2O_{7-\delta}$, Nat. Phys. **20**, 1269 (2024).

[16] Y. Meng, Y. Yang, H. Sun, S. Zhang, J. Luo, L. Chen, X. Ma, M. Wang, F. Hong, X. Wang, and X. Yu, Density-wave-like gap evolution in $La_3Ni_2O_7$ under high pressure revealed by ultrafast optical spectroscopy, Nat. Commun. **15**, 10408 (2024).

[17] M. Zhang, C. Pei, Q. Wang, Y. Zhao, C. Li, W. Cao, S. Zhu, J. Wu, and Y. Qi, Effects of pressure and doping on Ruddlesden-Popper phases $La_{n+1}Ni_nO_{3n+1}$, J. Mater. Sci. Technol. **185**, 147 (2024).

[18] R. Khasanov, T. J. Hicken, D. J. Gawryluk, V. Sazgari, I. Plokhikh, L. P. Sorel, M. Bartkowiak, S. Bötzel, F. Lechermann, I. M. Eremin, H. Luetkens, and Z. Guguchia, Pressure-enhanced splitting of density wave transitions in $La_3Ni_2O_{7-\delta}$, Nat. Phys. **21**, 430 (2025).

[19] G. Wu, J. J. Neumeier, and M. F. Hundley, Magnetic susceptibility, heat capacity, and pressure dependence of the electrical resistivity of $La_3Ni_2O_7$ and $La_4Ni_3O_{10}$, Phys. Rev. B **63**, 245120 (2001).

[20] N. K. Gupta, R. Gong, Y. Wu, M. Kang, C. T. Parzyck, B. Z. Gregory, N. Costa, R. Sutarto, S. Sarker, A. Singer, D. G. Schlom, K. M. Shen, and D. G. Hawthorn, Anisotropic spin stripe domains in bilayer $La_3Ni_2O_7$, Nat. Commun. **16**, 6560 (2025).

[21] M. Li, M. Zhang, Y. Wang, J. Guan, N. Li, C. Pei, N.-D. Adama, Q. Kong, Y. Qi, and W. Yang, Orbital signatures of density wave transition in $La_3Ni_2O_{7-\delta}$ and $La_2PrNi_2O_{7-\delta}$ RP-nickelates probed via *in-situ* X-ray absorption near-edge spectroscopy, arXiv:2502.10962.

[22] K. Chen, X. Liu, J. Jiao, M. Zou, C. Jiang, X. Li, Y. Luo, Q. Wu, N. Zhang, Y. Guo, *et al.*, Evidence of spin density waves in $La_3Ni_2O_{7-\delta}$, Phys. Rev. Lett. **132**, 256503 (2024).

[23] M. Kakoi, T. Oi, Y. Ohshita, M. Yashima, K. Kuroki, T. Kato, H. Takahashi, S. Ishiwata, Y. Adachi, N. Hatada, T. Uda, and H. Mukuda, Multiband metallic ground state in multilayered nickelates $La_3Ni_2O_7$ and $La_4Ni_3O_{10}$ probed by ^{139}La−NMR at ambient pressure, J. Phys. Soc. Jpn. **93**, 053702 (2024).

[24] D. Zhao, Y. Zhou, M. Huo, Y. Wang, L. Nie, Y. Yang, J. Ying, M. Wang, T. Wu, and X. Chen, Pressure-enhanced spin-density-wave transition in double-layer nickelate $La_3Ni_2O_{7-\delta}$, Sci. Bull. **70**, 1239 (2024).

[25] J. M. Tranquada, B. J. Sternlieb, J. D. Axe, Y. Nakamura, and S. Uchida, Evidence for stripe correlations of spins and holes in copper oxide superconductors, Nature (London) **375**, 561 (1995).

[26] Z. Guguchia, D. Das, C. N. Wang, T. Adachi, N. Kitajima, M. Elender, F. Brückner, S. Ghosh, V. Grinenko, T. Shiroka, *et al.*, Using uniaxial stress to probe the relationship between competing superconducting states in a cuprate with spin-stripe order, Phys. Rev. Lett. **125**, 097005 (2020).

[27] M. Smidman, Magnetic order sets the stage, Nat. Phys. **21**, 338 (2025).

[28] M. Shi, D. Peng, Y. Li, S. Yang, Z. Xing, Y. Wang, K. Fan, H. Li, R. Wu, B. Ge, Z. Zeng, Q. Zeng, J. Ying, T. Wu, and X. Chen, Spin density wave rather than tetragonal structure is prerequisite for superconductivity in $La_3Ni_2O_{7-\delta}$, Nat. Commun. **16**, 9141 (2025).

[29] T. Xie, M. Huo, X. Ni, F. Shen, X. Huang, H. Sun, H. C. Walker, D. Adroja, D. Yu, B. Shen, L. He, K. Cao, and M. Wang, Strong interlayer magnetic exchange coupling in $La_3Ni_2O_{7-\delta}$ revealed by inelastic neutron scattering, Sci. Bull. **69**, 3221 (2024).

[30] C. D. Ling, D. N. Argyriou, G. Wu, and J. J. Neumeier, Neutron diffraction study of $La_3Ni_2O_7$: Structural relationships among $n = 1, 2$, and 3 phases $La_{n+1}Ni_nO_{3n+1}$, J. Solid State Chem. **152**, 517 (2000).

[31] V. I. Voronin, I. F. Berger, V. A. Cherepanov, L. Y. Gavrilova, A. N. Petrov, A. I. Ancharov, B. P. Tolochko, and S. G. Nikitenko, Neutron diffraction, synchrotron radiation and EXAFS spectroscopy study of crystal structure peculiarities of the lanthanum nickelates $La_{n+1}Ni_nO_y$ ($n = 1, 2, 3$), Nucl. Instrum. Methods Phys. Res., Sect. A **470**, 202 (2001).

[32] J. Zhang, D. Phelan, A. S. Botana, Y.-S. Chen, H. Zheng, M. Krogstad, S. G. Wang, Y. Qiu, J. A. Rodriguez-Rivera, R. Osborn, S. Rosenkranz, M. R. Norman, and J. F. Mitchell, Intertwined density waves in a metallic nickelate, Nat. Commun. **11**, 6003 (2020).

[33] R. Misawa, S. Kitou, J.-P. Sun, Y. Yu, C. Koyama, Y. Nakamura, T.-H. Arima, J.-G. Cheng, and M. Hirschberger, Polar, checkerboard charge order in bilayer nickelate $La_3Ni_2O_7$, arXiv:2603.25119.

[34] K. W. Chen, X. Q. Liu, Y. Wang, Z. Y. Zhu, J. C. Jiao, C. Y. Jiang, Y. F. Guo, and L. Shu, Evolution of magnetism in Ruddlesden-Popper bilayer nickelate revealed by muon spin relaxation, arXiv:2412.09003.

[35] R. Khasanov, I. Plokhikh, T. J. Hicken, H. Luetkens, D. J. Gawryluk, and Z. Guguchia, Pressure effect on the spin density wave transition in $La_2PrNi_2O_{6.96}$, Phys. Rev. Res. **7**, L022046 (2025).

[36] K. Momma and F. Izumi, VESTA 3 for three-dimensional visualization of crystal, volumetric and morphology data, J. Appl. Crystallogr. **44**, 1272 (2011).

[37] R. Khasanov, T. J. Hicken, H. Luetkens, Z. Guguchia, D. J. Gawryluk, V. Sundaramurthy, A. Suthar, M. Isobe, B. Keimer, G. Khaliullin, M. Hepting, and P. Puphal, Magnetism of the alternating monolayer-trilayer phase of $La_3Ni_2O_7$, arXiv:2512.22371 [cond-mat.supr-con].

[38] A. Furrer, J. Mesot, and T. Strässle, *Neutron Scattering in Condensed Matter Physics* (World Scientific, Singapore, 2009), Vol. 4, p. 301.

[39] R. Khasanov, V. Sazgari, T. J. Hicken, I. Plokhikh, M. Medarde, E. Pomjakushina, L. Keller, V. Pomjakushin, M. Bartkowiak, S. Królak, M. J. Winiarski, A. Steppke, J. A. Krieger, H. Luetkens, T. Klimczuk, C. W. Schneider, D. J. Gawryluk, and Z. Guguchia, Pressure and oxygen-isotope substitution on density-wave transitions in $La_4Ni_3O_{10}$, Phys. Rev. Res. **8**, 013249 (2026).

[40] M. S. Henriques, V. Petříček, S. Goswami, and M. Dušek, Analysis of magnetic structures in JANA2020, Acta Crystallogr. B: Struct Sci. Cryst. Eng. Mater. **80**, 409 (2024).

[41] V. Petříček, L. Palatinus, J. Plášil, and M. Dušek, JANA2020—A new version of the crystallographic computing system JANA, Z. Kristallogr. Cryst. Mater. **238**, 271 (2023).

[42] H. T. Stokes, D. M. Hatch, and B. J. Campbell, ISODISTORT, ISOTROPY software suite, https://iso.byu.edu.

[43] B. J. Campbell, H. T. Stokes, D. E. Tanner, and D. M. Hatch, ISODISPLACE: An internet tool for exploring structural distortions, J. Appl. Crystallogr. **39**, 607 (2006).

[44] J. M. Perez-Mato, S. V. Gallego, E. S. Tasci, L. Elcoro, G. de la Flor, and M. I. Aroyo, Symmetry-based computational tools for magnetic crystallography, Annu. Rev. Mater. Res. **45**, 217 (2015).

[45] J. M. Perez-Mato, S. V. Gallego, L. Elcoro, E. S. Tasci, and M. I. Aroyo, Symmetry-based computational tools for magnetic crystallography, J. Phys.: Condens. Matter **28**, 286001 (2016).

[46] A. P. Cracknell, B. L. Davies, S. C. Miller, and W. F. Love, *Kronecker Product Tables, Vol. 1: General Introduction and Tables of Irreducible Representations of Space Groups* (IFI/Plenum, New York, 1979).

[47] M. I. Aroyo, D. Orobengoa, G. de la Flor, E. S. Tasci, J. M. Perez-Mato, and H. Wondratschek, Brillouin-zone database on the Bilbao crystallographic server, Acta Crystallogr. A: Found. Adv. **70**, 126 (2014).

[48] J. M. Perez-Mato, B. J. Campbell, V. O. Garlea, F. Damay, G. Aurelio, M. Avdeev, M. T. Fernández-Díaz, M. S. Henriques, D. Khalyavin, S. Lee, *et al.*, Guidelines for communicating commensurate magnetic structures: A report of the International Union of Crystallography Commission on Magnetic Structures, Acta Crystallogr. B: Struct. Sci. Cryst. Eng. Mater. **80**, 219 (2024).

[49] B. J. Campbell, H. T. Stokes, J. M. Perez-Mato, and J. Rodríguez-Carvajal, Introducing a unified magnetic space-group symbol, Acta Crystallogr. A: Found. Adv. **78**, 99 (2022).

[50] Z. Dong, G. Wang, N. Wang, W.-H. Dong, L. Gu, Y. Xu, J. Cheng, Z. Chen, and Y. Wang, Interstitial oxygen order and its competition with superconductivity in $La_2PrNi_2O_{7+\delta}$, Nat. Mater. **24**, 1927 (2025).

[51] X.-S. Ni, Y. Ji, L. He, T. Xie, D.-X. Yao, M. Wang, and K. Cao, Spin density wave in the bilayered nickelate $La_3Ni_2O_{7-\delta}$ at ambient pressure, npj Quantum Mater. **10**, 17 (2025).

[52] Paul Scherrer Institute, DMC—Cold neutron powder diffractometer, https://www.psi.ch/en/sinq/dmc.

[53] M. Yashima, N. Seto, Y. Oshita, M. Kakoi, H. Sakurai, Y. Takano, and H. Mukuda, Microscopic evidence for spin–spinless stripe order with reduced Ni moments within *ab* plane for bilayer nickelate $La_3Ni_2O_7$ probed by ^{139}La-NQR, J. Phys. Soc. Jpn. **94**, 054704 (2025).

[54] K. Foyevtsova, I. Elfimov, and G. A. Sawatzky, Charge distribution and magnetism in bilayer $La_3Ni_2O_7$: A hybrid functional study, Phys. Rev. B **112**, 235163 (2025).

[55] G. Jiang, C. Qin, K. Foyevtsova, L. Si, M. Berciu, G. A. Sawatzky, and M. Jiang, Intertwined charge and spin instability of $La_3Ni_2O_7$, Sci. China Phys. Mech. Astron. **68**, 297411 (2025).

[56] I. Plokhikh, V. Pomjakushin, D. J. Gawryluk, O. Zaharko, and E. Pomjakushina, Competing magnetic phases in *Ln*SbTe (*Ln* = Ho and Tb), Inorg. Chem. **61**, 11399 (2022).

[57] I. Plokhikh, O. Fabelo, L. Prodan, M. Wörle, E. Pomjakushina, A. Cervellino, V. Tsurkan, I. Kézsmárki, and O. Zaharko, Magnetic and crystal structure of the antiferromagnetic skyrmion candidate $GdSb_{0.71}Te_{1.22}$, J. Alloys Compd. **936**, 168348 (2023).

[58] I. Plokhikh, V. Pomjakushin, D. J. Gawryluk, O. Zaharko, and E. Pomjakushina, On the magnetic structures of 1:1:1 stoichiometric topological phases *Ln*SbTe (*Ln* = Pr, Nd, Dy, and Er), J. Magn. Magn. Mater. **583**, 171009 (2023).

[59] Z. Sun, C. Hong, Y. Chen, Z. Sheng, S. Wu, Z. Wang, B. Liang, W.-T. Liu, Z. Yuan, Y. Wu, *et al.*, Resolving and routing

magnetic polymorphs in a 2D layered antiferromagnet, Nat. Mater. **24**, 226 (2025).

[60] S. Akatsuka, S. Esser, S. Okumura, R. Yambe, R. Yamada, M. M. Hirschmann, S. Aji, J. S. White, S. Gao, Y. Onuki, T.-h. Arima, T. Nakajima, and M. Hirschberger, Non-coplanar helimagnetism in the layered van-der-Waals metal $DyTe_3$, Nat. Commun. **15**, 4291 (2024).

[61] R. Khasanov, V. Sazgari, I. Plokhikh, L. Shi, K. Ma, M. Medarde, E. Pomjakushina, T. Klimczuk, T. J. Hicken, H. Luetkens, C. W. Schneider, Z. Guguchia, S. Medvedev, and D. J. Gawryluk, Oxygen-isotope effect on the density wave transitions in $La_3Ni_2O_7$, Phys. Rev. Res. **8**, L012055 (2026).

[62] J. Schefer, P. Fischer, H. Heer, A. Isacson, M. Koch, and R. Thut, A versatile double-axis multicounter neutron powder diffractometer, Nucl. Instrum. Methods Phys. Res., Sect. A **288**, 477 (1990).

[63] P. Fischer, G. Frey, M. Koch, M. Könnecke, V. Pomjakushin, J. Schefer, R. Thut, N. Schlumpf, R. Bürge, U. Greuter, *et al.*, High-resolution powder diffractometer HRPT for thermal neutrons at SINQ, Physica B **276–278**, 146 (2000).

[64] A. Amato, H. Luetkens, K. Sedlak, A. Stoykov, R. Scheuermann, M. Elender, A. Raselli, and D. Graf, The new versatile general purpose surface-muon instrument (GPS) based on silicon photomultipliers for μSR measurements on a continuous-wave beam, Rev. Sci. Instrum. **88**, 093301 (2017).

[65] Paul Scherrer Institute, FLAME Project—Muon Spin Spectroscopy, 2025, accessed 11 February 2025, www.psi.ch/en/smus/flame-project.

[66] A. Suter and B. M. Wojek, Musrfit: A free platform-independent framework for μSR data analysis, Phys. Procedia **30**, 69 (2012).

[67] R. Kubo and T. Toyabe, in *Proceedings of the 14th Colloque Ampère* (North-Holland, 1967), pp. 810–823.

[68] P. Bonfà, I. J. Onuorah, and R. De Renzi, Introduction and a quick look at MUESR, the Magnetic structure and mUon Embedding Site Refinement suite, JPS Conf. Proc. **21**, 011052 (2018).

[69] L. Chen, E. Zhang, Y. Hao, Y. Zhu, B. Cui, D. L. Abernathy, T. J. Williams, Y. Ikeda, H. Zhang, F. Liu, W. Wang, Q. Wang, and J. Zhao, Nature of magnetism in bilayer nickelate $La_3Ni_2O_7$ single crystals, arXiv:2605.03448.